Colloid and Interface Science Communications 49 (2022) 100641

Contents lists available at ScienceDirect

Colloid and Interface Science Communications

journal homepage: www.elsevier.com/locate/colcom

Short Communication

Particle sizing in non-dilute dispersions using diffusing wave spectroscopy with multiple optical path lengths

Robert E. McMillin [a], Davide Orsi [b], Luigi Cristofolini [b], James K. Ferri [a,*]

[a] Virginia Commonwealth University Department of Chemical and Life Science Engineering, Richmond,VA, United States of America
[b] University of Parma Department of Mathematical, Physical and Computer Sciences, Parma, Italy

ARTICLE INFO

Keywords:
Light scattering
Diffusing wave spectroscopy
DWS
Suspension
Particle sizing
Non-dilute dispersions

ABSTRACT

Non-dilute dispersed phase systems, such as foams, emulsions, and suspensions, are an important class of final formulations and chemical process intermediates in a variety of industries. The utility of these systems hinges on their stability over the lifetime of use, and therefore an accurate assessment of chemical and physical dynamics, asformulated, is required. We describe a unified treatment of diffusing wave spectroscopy (DWS) data using a range of optical path length with a goniometric instrument. DWS correlation data from multiple angles and robust Monte Carlo simulations are used to determine accurate values of the photon transport mean free path length. The variance on each correlation function is used to determine the physical time range that the mean squared displacement can be analyzed. Using standard solid particle suspensions of polystyrene and SiO2, we determine the average particle size with accuracy comparable to dynamic light scattering.

1. Introduction

Disperse systems, such as emulsions, foams, and suspensions, are important intermediate and final formulations in a variety of science and technology applications. For example, emulsions are used in applications ranging from the food and pharmaceutical industry to paints and coatings [1,2]. Likewise, particle suspensions are the basis of latex paints and can be used to enhance pharmaceutical bioavailability in liquid dose forms [3]. The stability of these formulations is often inferred from idealized measurements of the evolution of the mean size or from the overall rheology of the system.

In the dilute limit, the behavior of a dispersion can be probed directly using dynamic light scattering (DLS) or microscopy to determine average droplet sizes [4,5]. However in concentrated dispersions, in-situ droplet or particle size measurements are difficult to obtain without compromising sample integrity. Diffusing wave spectroscopy (DWS) offers a potential solution to this challenge. DWS is a photon correlation spectroscopy technique which approximates light traveling through the sample as a diffusion process. This method has been successfully applied to study relative changes in structure as well as the rheology of optically dense systems, including particle suspensions, foams, and emulsions [6–10]. However, it commonly asserted that DWS performs poorly at particle sizing [11].

In a typical DWS experiment, coherent laser light impinges on a highly multiple-scattering sample. Scattered light is then detected in the far field and the intensity fluctuations (caused by the motion of scattering of centers, e.g., droplets, bubbles, or solid particles) are temporally correlated yielding the intensity autocorrelation function, $g_2(\tau)$ [11].

The collection optics used are predominantly avalanche photodiodes (APDs) or photomultiplier tubes (PMTs) (for single-speckle detection), though a camera can also be used to determine $g_2(\tau)$ (multi-speckle) as well [12]. Before yielding interprable information on the scattering centers, the intensity autocorrelation function, $g_2(\tau)$ must be transformed to the electric field autocorrelation function, $g_1(\tau)$ via the Siegert relation, assuming Gaussian statistics [13]:

$$|g_1(\tau)|^2 = \frac{1}{\beta}(g_2(\tau) - 1) \quad (1)$$

The parameter β is the contrast and depends on the experimental setup. The light propagation is treated as a diffusion process, it is assumed to undergo a random walk through the sample. Each photon can thus take a path of length s with an average step length of l^*, called the transport mean free path [14]. $g_1(\tau)$ is then the sum of all autocorrelations corresponding to all possible path lengths, s, weighted by the probability, $P(s)$, of a photon taking a path of that length [14]:

* Corresponding author.
E-mail addresses: mcmillinre@vcu.edu (R.E. McMillin), davide.orsi@unipr.it (D. Orsi), luigi.cristofolini@unipr.it (L. Cristofolini), jkferri@vcu.edu (J.K. Ferri).

https://doi.org/10.1016/j.colcom.2022.100641
Received 10 May 2022; Received in revised form 10 June 2022; Accepted 13 June 2022

$$g_1(\tau) = \int_0^\infty P(s) e^{-k_0^2 \left\langle \Delta r^2(\tau) \right\rangle \frac{s}{3l^*}} ds \tag{2}$$

Where k_0 is the incident wave vector, given by $k_0 = 2\pi n/\lambda$, and $\langle \Delta r^2(\tau) \rangle$ is the mean squared displacement over all scattering centers illuminated by the impinging beam at a lag time τ.

Both the transport mean free path, l^*, and the mean squared displacement offer insights into the physical nature of the dispersed system. For example, Sun et al., was able to discern the relative differences in elasticity of two emulsion formulations by analyzing the mean squared displacement [15]. By studying the trends in mean squared displacement over ageing for the two formulations, the authors could conclude the main factors impacting storage stability. Likewise, l^* can also be used to discern physical processes in dispersed phase systems. In a study on the effects of pH on the dynamics of association in emulsions, l^* was used to confirm disruption of micelles upon re-equilibration after the pH was altered [16].

While the physical interpretations of l^* and the mean squared displacement are useful in understanding dispersed phase systems, the extraction of these parameters is not straightforward. For example, Eq. 2, shows they are fully confounded. Furthermore, in order to extract any parameters from $g_1(\tau)$, the path length distribution must be known. Therefore, utilizing DWS to study a system requires the solution to those two key problems.

The path length distribution, $P(s)$ is a function of both l^* and the experimental geometry of the DWS apparatus, namely the location of the detector relative to the incident light, the shape of the sample cell, and the distribution of light on the surface of the cell. The two most frequent locations of detectors are across the sample, opposite of the impinging beam, (transmission, Scheme 1A2) or on the same side of the sample as the impinging beam (backscattering, Scheme 1A1).

Commonly, a sample cell with a semi-infinite domain is used, where the cell is rectangular in shape and the dimensions perpendicular to the incident light are much larger than the thickness, L, of the cell, lying parallel to the incident beam, shown in Scheme 1A. In this case, the light is assumed to diffuse finitely in only one direction, and can be easily described by the diffusion equation [11]. If the impinging beam is expanded to cover the entire incident surface, called the 'plane wave approximation', and the detector is in the transmission orientation, $P(s)$ takes the form [17]:

$$P(s) = \frac{\sqrt{3}}{\sqrt{4\pi s l^*}} \sum_{n=-\infty}^{\infty} \left\{ exp\left[\frac{-3((2n-1)L - 2l^*)^2}{4sl^*} \right] - exp\left[\frac{-3\left((2n-1)L^2\right)^2}{4sl^*} \right] \right\} \tag{3}$$

Eq. 3 can be substituted into Eq. 2 to yield an analytical expression for $g_1(\tau)$ dependent only upon L, l^*, and the mean squared displacement. Similar solutions can be found for an incident point source and Gaussian beam, as well as corresponding backscattering detector orientations [6]. For geometries that cannot be approximated as 1D diffusion, a general analytical solution to Eq. 2 has not been achieved. An example of a non-conforming geometry is shown in Scheme 1B, where the sample cell is cylindrical and the detector is located at an angle θ from the normal. Despite this, researchers have utilized stochastic simulations to determine $P(s)$ for their specific experimental geometry with good agreement between theoretical and experimentally determined $g_1(\tau)$ [18,19]. Typically, numerical simulations are performed where photons undergo a 3D random walk through a volume approximating the sample cell or through a 2D random walk in a planar projection of the sample cell. In the latter case, used by Fahimi et al. all to determine $P(s)$ for a cylindrical sample cell, an ideal probabilistic contribution is added to account for the diffusion in the dimension lost by projection [19].

After determining the path length distribution, either by the diffusion equation or by simulation, l^* and the mean squared displacement, $\langle \Delta r^2(\tau) \rangle$, can be extracted. The extraction process of these parameters requires careful consideration, however, since they are fully confounded. If the classical semi-infinite sample cell is utilized, both transmission and back-scattering data can be collected and used to separate them via the two independent equations [20]. Similarly, the temporally averaged intensity for transmission and back scattering can allow independent determination of l^* [21]. Calibration techniques have also been used to determine l^* in both classical geometries (e.g., finite light diffusion in a single dimension) and non-standard experimental setups. In the case of the commercially available DWS Rheolab instrument, manufactured by LS instruments, the average intensity of a calibration sample with a similar transport mean free path to that expected

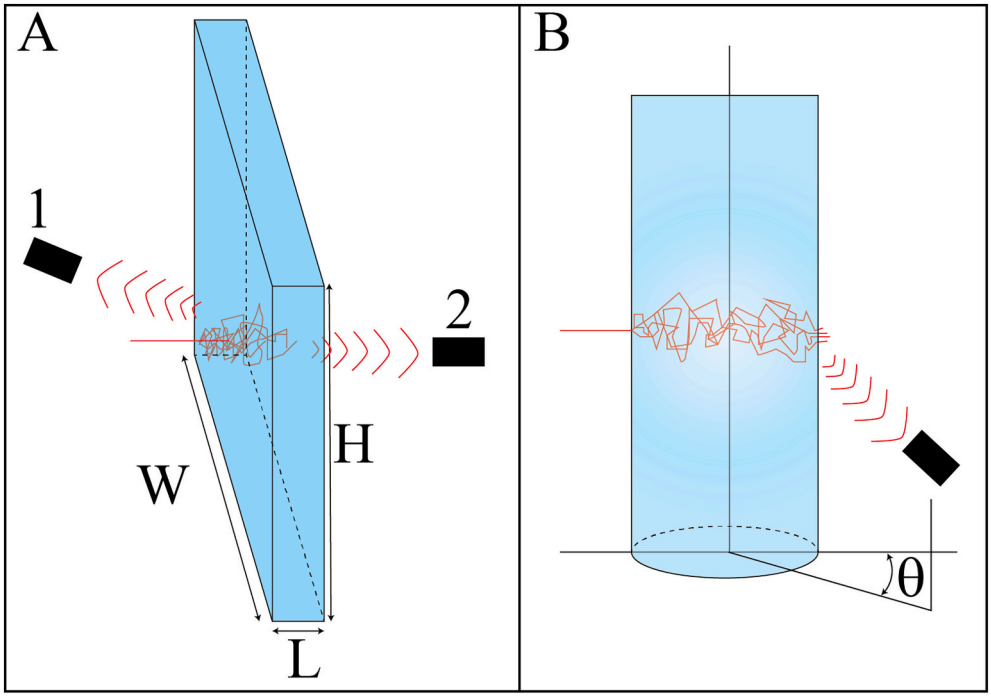

Scheme 1. DWS experimental setups. A) Classic semi-infinite domain DWS setup B) DWS performed on a cyclindrical sample cell

by the test sample is used to locally extrapolate an l^*. However, this method introduces an error between five and 10 % [21]. Lastly, for a non-standard DWS measurement in the ALV CGS-3 dynamic light scattering instrument, Fahimi et al. used an intensity calibration technique coupled with simulated l^* intensities [19]. The calibration was then used to determine l^* while using the same calibration particles as tracer particles to probe the microrheology of a non-Newtonian viscous medium.

Due to the variation of experimental setups, the different approaches to data analysis, and the range of sample features that can be studied, most analyses of DWS data are reported to perform poorly in particle sizing. This is due to the lack of a refined method focusing on the use of DWS for particle sizing. Herein, we report a standardized DWS data handling framework (shown in Fig. 1) to probe particle dynamics and determine particle size of dispersed systems on a non-standard goniometric DLS instrument. In this light, we propose systematic determinations of correlation error, contrast (β) determination, and statistically relevant regions of the mean squared displacement. We also introduce a robust calibration technique to determine l^* independently of sample dynamics combining methods from Fahimi et al. and Zhang et al. [19,21] Finally, we test our process on polystyrene and SiO_2 dispersions, achieving sizing accuracy typically exhibited by dedicated DLS instruments and microscopy, which may range from <1% to ~3% [22–24].

2. Experimental materials and methods

2.1. Solid suspensions

Polystyrene suspensions were prepared by diluting 514 nm, 1.02 μm, and 3.03 μm diameter 10 vol% size standards, obtained from Millipore Sigma, to final concentrations of 5%, 2.5%, 1.25%, and 0.625% in water. SiO_2 suspensions were prepared by dispersing dry 500 nm (General Engineering and Research), 1.0 μm (General Engineering and Research), and 4.3 μm (Cospheric) diameter spheres in water at 13, 10.8, 8.7, 6.5, and 4.3 wt% in water, followed by sonication for 5 min. In all cases, Ultrapure water (18.2 MΩ at 25 °C) was used from a MilliQ dispenser. Percent transmittance of the highest particle conentration (lowest l^*), lowest particle concentration (largest l^*), and mid point sample are shown in Section S5, verifying the optical density ($0.06 < \%T < 0.35\%$) for range of samples analyzed.

2.2. Diffusing wave spectroscopy experiments

Diffusing wave spectroscopy experiments were conducted on an ALV/CGS-3 Compact Goniometer from ALV-GmbH, equipped with a vertically polarized 633 nm 22 mW laser, two APD single-photon counters, an optical attenuator, and an ALV/LSE-5004 multiple τ correlator. Sample cuvettes for the instrument had an outer diameter of ~10 mm and an inner diameter of ~8.66 mm. The β_{exp} calibration experiments utilized the 514 nm and 1.02 μm polystyrene suspensions and the 500 nm and 1.0 μm SiO_2 suspensions at all concentrations. Each sample was run for a total collection time of 20 s at ten degree increments from 20 degrees to 150 degrees, for a total of 14 data sets per concentration and size. The test sets were conducted similarly with the 4.3 μm SiO_2 and 3.03 μm polystyrene spheres, however, they were only analyzed at 30, 90, and 150 degrees. The output of each light scattering experiment includes average intensity, an intensity time series, and intensity autocorrelation functions for each detector, and an attenuator value (as expressed via a monitor diode), used to correct intensity.

2.3. Data handling workflow

The goniometric instrument (ALV/CGS-3, ALV GmbH) allows the detectors to move in less than one degree increments around a cylindrical sample cell. Utilizing this feature, the input to our process is temporally averaged intensity, $\langle I(t)\rangle_\theta$, and intensity autocorrelation cuves, $g_2(\tau)_\theta$, for multiple angles. The raw $g_2(\tau)$ is converted to $g_1(\tau)$ and

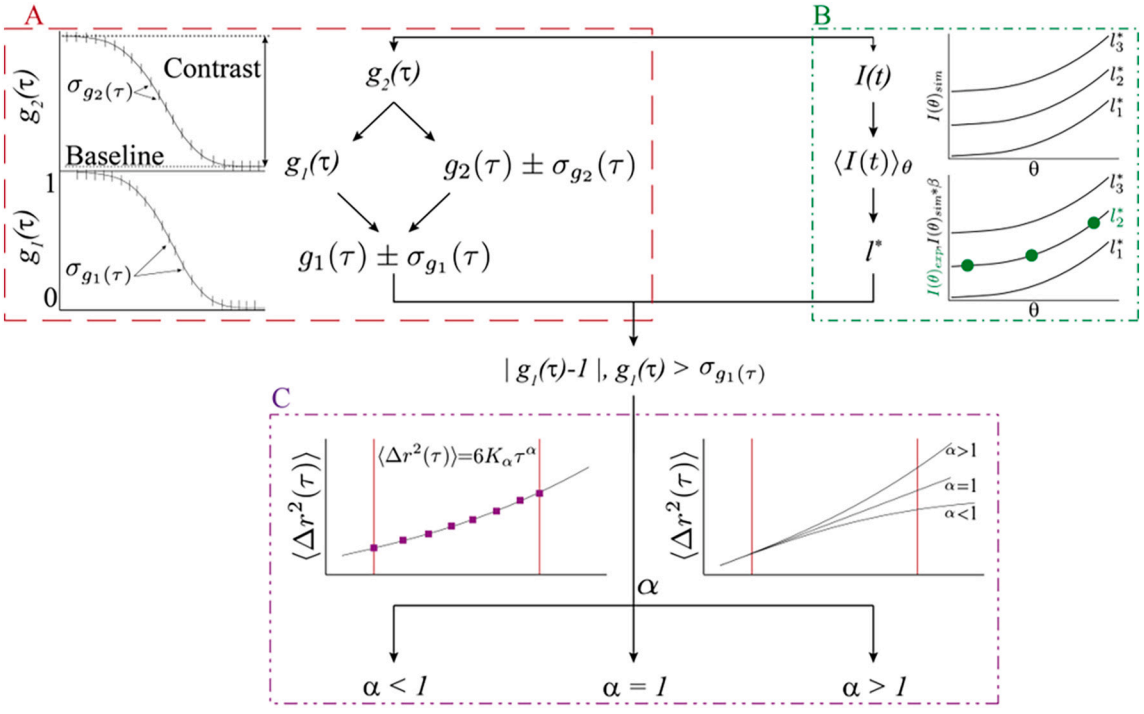

Fig. 1. Schematic overview of algorithmic treatment of DWS data to probe scattering center properties. A) From $g_2(\tau)$, the contrast and baseline are obtained in order to yield the electric field autocorrelation function, $g_1(\tau)$, as well as standard error B) l^* is determined after intensity calibration with ideal scattering centers, followed by a multi-angle simultaneous fit, and C) $g_1(\tau)$ data is filtered based upon its standard error to obtain a statistically relevant region of the mean squared displacement, $\langle \Delta r^2(\tau)\rangle$.

standard errors are calculated for all valid τ following the process outlined in Schätzel and Orsi et al., shown in Fig. 1A and described with an example in Section S2 [25,26]. Simultaneously, using the average intensity data, an l^* is determined through fitting to a multi-angle simulation intensity curve, shown in Fig. 1B and elaborated on in Section S3. The resulting $g_1(\tau)$ data is filtered based upon the standard error at each τ and a region is selected where the correlation function is statistically different than one and zero. This region defines the portion of the curve where statistically significant physical results can be extracted.

Using the l^* determined in Fig. 1B and $g_1(\tau)$, the nominal mean squared displacement, $\langle \Delta r^2(\tau) \rangle$ is extracted. The standard error from $g_1(\tau)$, $\sigma_{g1}(\tau)$, is similarly propagated through the numerical extraction yielding $\sigma_{MSD}(\tau)$, described in more detail in Section S4. Shown in Fig. 1C., the region identified by the error on $g_1(\tau)$ is fit to an anomalous diffusion model, $\langle \Delta r^2(\tau) \rangle = 6K_\alpha \tau^\alpha$, where the value of α describes the motion of the dispersed phase as being Brownian ($\alpha = 1$), super-diffusive ($\alpha > 1$), or sub-diffusive ($\alpha < 1$). Depending on this value, a more appropriate model of the mean squared displacement is used to extract physical parameters associated with the sample, such as particle/droplet size [27].

3. Results and discussion

3.1. Stochastic simulations

In order to determine $P(s)$ for a cylindrical sample cell, we utilized stochastic simulations similar to Lorusso et al. and Fahimi et al. [18,19] Photons were numerically simulated in a 3D Cartesian coordinate space with a cylindrical bounding surface approximating the cuvettes radius (R) and height (z_{max}), shown in Fig. 2A, where $P(s)$ must be determined for all detection angles, n_θ, of interest. The photons were assumed to undergo an ideal random walk in all dimensions with an average step length of l^*. The laser impinges on the sample cell ~5 mm (z_{min}) from the base of the cuvette without beam expansion. Thus, the numerical simulation starts each photon at ($x = -R + l^*, y = 0, z = 0$) and photons are allowed to randomly walk until $x^2 + y^2 \geq R^2$ or $z \leq z_{min} \vee z \geq z_{max}$. Similar to Fahimi et al., we set a z detection limit corresponding to the number of angular detection bins, $|z| < \frac{\pi}{2n_\theta}$ [19]. In all simulations we set a one degree angular resolution for a total $n_\theta = 180$. If a photon reaches the surface of the cylinder within the z detection criteria, the angle and total number of steps, N, is recorded. Any photon exiting that does not meet the z criteria is discarded. Photons that reach the z_{min} or z_{max} criteria are assumed to exit the sample without detection and also go unrecorded.

In an unrestricted random walk, the number of expected steps is equal to $N_{exp} = L^2/l^{*2}$, where L is the magnitude of displacement and shown in Fig. 2A. We determine the distribution of N by binning detected photons in 400 linearly spaced bins beginning at $N_{min} = N_{exp}/100$ and extending to 400 * N_{min}. $P(s)$ is then calculated by multiplying the bins by l^* and normalized such that $\int_0^\infty P(s)\,ds = 1$. Example $P(s)$ curves for a simulated l^* of 500 μm are shown in Fig. 2B alongside corresponding ideal calculated $P(s)$ curves from Eq. 3 using the calculated L. The simulated path length distributions are distinctly different than those calculated from Eq. 3. Fig. 2C shows L (left axis, red), as well as N (right axis, blue) for an ideal random walk (solid line, N_exp) and the simulated photons (symbols, calculated by ($N_{sim} = \int_0^\infty P(s) s\,ds/l^*$)). Due to the differences in calculated and simulated probabilities, it is evident that simulations are required to adequately describe the diffusion of light through a cylindrical sample cell. Interestingly, for angles $\theta < 120^o$ the calculated average number of scattering events is less than N_{exp}, however at $\theta = 120^o$, where $L = R$, a cross over occurs and $N_{sim} > N_{exp}$. In contrast to Fahimi et al., we did not find that $P(s)$ could be scaled by the average path length to yield a 'master curve [19].' To mitigate this, we created a library of simulated $P(s)$ series at all angles with l^*/R ranging from 5×10^{-4} to ~0.35 in increments of 5×10^{-4}. This gave us 2.5 μm resolution on calculated values of l^*, which we found more than adequate given experimental uncertainty with respect to particle concentration.

3.2. Variance on autocorrelation functions

In order to use the Siegert relation, Eq. 1, to obtain $g_1(\tau)$ from $g_2(\tau)$ the values of the baseline and contrast, β, should be obtained as accurately as possible. Importantly, the parameter β has implications on the signal to noise ratio in a DWS experiment where a larger value of β corresponds to a decrease in the signal-to-noise ratio. Incorrectly determining β can distort the variance, and therefore accuracy, of the correlation functions.

In Fig. 3A, we schematically show the values of the baseline, intercept, and contrast on a typical $g_2(\tau)$ curve. The intercept is the short-time limiting value of the curve, the baseline is the long-time limiting value of the curve, and the contrast, β, is the difference between the intercept and baseline. To determine the intercept value, a model exponential decay function is fit to $g_2(\tau)$ [26]. Baseline determination, however, can be more difficult. Often, the average value of $g_2(\tau)$ is taken at the final lag times measured, however, for samples exhibiting slow dynamics, it is difficult to determine where stationarity in $g_2(\tau)$ has been reached. Rather than taking an average over a prescribed range, we instead model

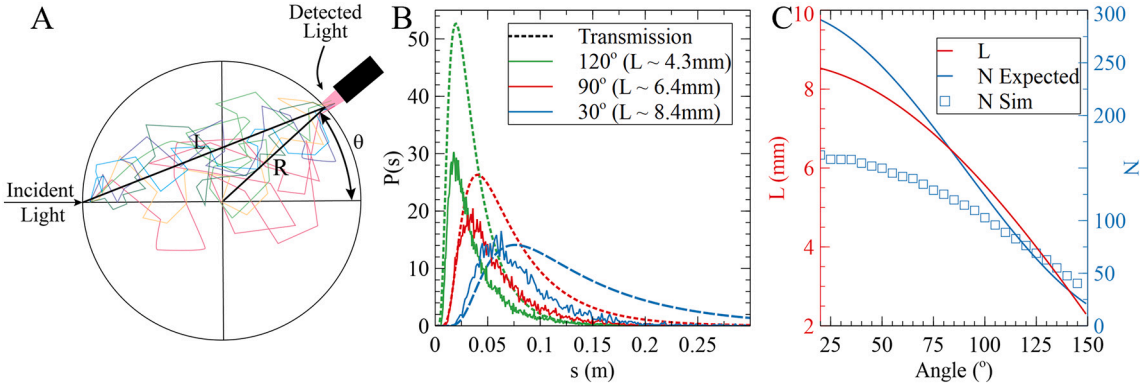

Fig. 2. Stochastic simulations were performed in order to obtain the path length distribution, P(s) for each possible angle of detection. A) 2D cross section of the 3D stochastic simulations in a cylindrical sample cell, B) simulated and calculated (via the diffusion approximation for a semi-infinite domain) path length distributions for detection angles of 30, 90, and 120 degrees. The corresponding sample thickness (L) was used for the calculated path length distribution and all curves utilize an l^* of 500 μm. C) Geometrically calculated L equivalent as a function of detection angle shown on the left axis. The expected number of average scattering events (line), $N = L^2/l^{*2}$ is shown on the right axis, as well as the simulated average number of scattering events (squares).

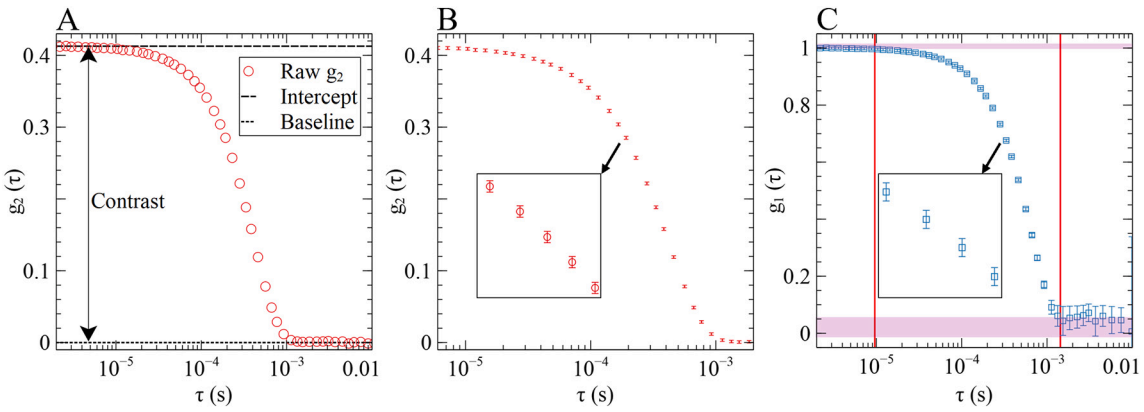

Fig. 3. Determination of σ_τ for $g_2(\tau)$ and $g_1(\tau)$. A) Graphical representation of the baseline, intercept, and contrast values that are required to transform $g_2(\tau)$ to $g_1(\tau)$ via the Siegert relation. B) $g_2(\tau)$ and $\sigma_{g2}(\tau)$ calculated via the Siegert relation and corresponding baseline and contrast values determined from A. C) $g_1(\tau)$ shown with $\sigma_{g1}(\tau)$ determined via the propagation of error from $g_2(\tau)$ in the Siegert relation. The region between the vertical red bars represents the region where $g_1(\tau)$ is statistically different from 1 and 0. (For interpretation of the references to colour in this figure legend, the reader is referred to the web version of this article.)

the first differences of $g_2(\tau)$ as a convergent geometric series, i.e. $g_2(\tau)_{i-1} - g_2(\tau)_{i-1} = ar^i$, beginning at the 50% decay point. The series approximation has a well-defined convergent sum which can then be used to calculate the long time limiting value of $g_2(\tau)$, reducing the impact of noise at large lag times.

With the baseline and intercept values the contrast is calculated and used to determine the variance on $g_2(\tau)$ as shown by Orsi et al. [26] In short, the variance is estimated as a function of photon noise and signal noise. Both sources of noise may contribute to the total variance and are functions of the average photon counts per frame and the number of correlated pairs. A more in depth discussion of the variance can be found in Schätzel and Orsi et al. [25,26] The variance is calculated and converted to standard error for all lag times in $g_2(\tau)$, shown in Fig. 3B. Once the error on $g_2(\tau)$ is determined, we use Eq. 1 to convert $g_2(\tau) \pm \sigma_{g2}(\tau)$ to $g_1(\tau) \pm \sigma_{g1}(\tau)$, shown in Fig. 3C. $g_1(\tau)$ is further filtered based upon its error. The intercept and baseline for $g_1(\tau)$ are unity and zero, respectfully, therefore, we consider any value $g_1(\tau) < \sigma_{g1}(\tau)$ or $|g_1(\tau) - 1| < \sigma_{g1}(\tau)$ to be statistically indistinguishable from the short and long time limiting values. In Fig. 3 the vertical lines denote where these cut offs occur and the highlighted regions represent the range of error. Any $g_1(\tau)$ within the red vertical lines can therefore be utilized to extract physical information with statistical certainty.

3.3. Transport mean free path (l^*) calibration

To obtain physical information about the dynamics of a sample from Eq. 2, l^* must be known. Likewise, if the dynamics of a sample are known, then l^* can be determined. We, similar to Fahimi et al., approach this confounding of optical and physical properties in two steps [19]. First, we determine l^*, using Eq. 2 and simulated P(s), on model suspensions (e.g. $\langle \Delta r^2(\tau) \rangle = 6D\tau$) with various particle concentrations, sizes, and refractive indexes. We then compare the simulated intensity for the best fit l^* with the measured intensity to determine an experimental constant, β_{exp}, which can be used to determine l^* from a sample with unknown dynamics from intensity alone.

The calibration samples were made as outlined in Section 2.1 using 514 nm and 1.02 μm polystyrene particles and 500 nm and 1.0 μ SiO_2 particles. The concentrations of each sample were varied to span a large range of possible l^* values. For each sample, $g_2(\tau)$ and the average intensity was obtained for angles spanning 20^o to 150^o in 10^o increments. Thus a single calibration measurement consisted of 14 angles with two measurements at each angle. For each angle, $g_2(\tau)$ was converted to $g_1(\tau)$ and fit using Eq. 2 with the corresponding P(s) distribution. During fitting, the particles were assumed to freely diffuse, thus the mean squared displacement could be approximated as $\langle \Delta r^2(\tau) \rangle = 6D\tau$, and the only adjustable parameter was l^*. In Fig. 4A we show experimental $g_1(\tau)$ (symbols) along with fitted curves using Eq. 2 for $\theta = 90^o$. The data corresponds well to theory, showing our simulated P(s) can adequately describe correlation functions in goniometric DWS. Furthermore, the agreement between theory and experiment is uniform across the SiO_2 (circles) and polystyrene (squares) dispersions, indicating both sets of particles exhibited Brownian motion. The value of l^* determined at each angle is relatively constant and therefore we take the numerical average across all angles as the best fit l^* for each calibration sample.

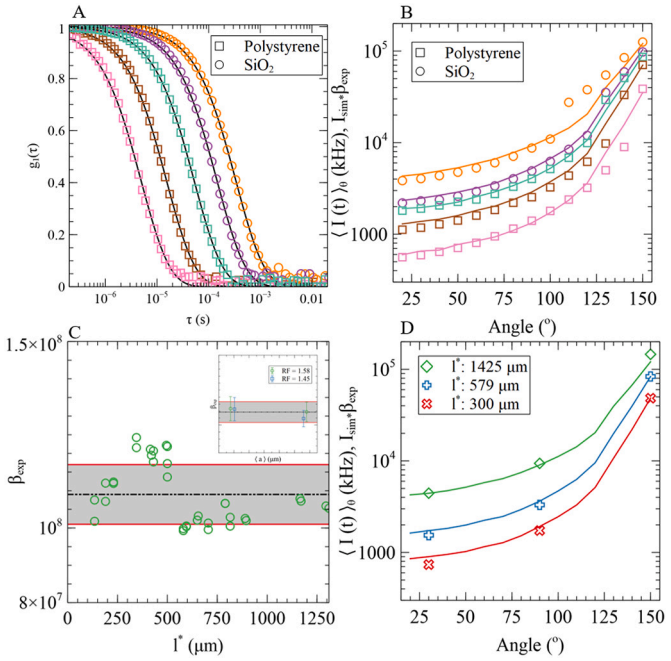

Fig. 4. Intensity calibration from ideal scattering centers. A) $g_1(\tau)$ for five calibration samples measured at 90 degrees with fitted curves using Eq. 2. 1.02 μm polystyrene particles (squares) at 2.5, 1.25, and 0.625 vol% and 1.0 μm SiO_2 particles at 8.7 and 6.5 wt% B) Intensity as a function of detector angle for the suspensions utilized in A. C) β_{exp} as a function of fitted l^* for all calibration samples and β_{exp} grouped by particle radius and particle refractive index (inset). D) Measured intensity at 30, 90 and 150 degrees for 4.3 μm SiO_2 suspensions (check samples on calibration) at 13, 10.8, and 8.7 wt% (symbols) and simulated intensity scaled by the average β_{exp} determined from C at l^* values of 300 μm, 579 μm, and 1425 μm (lines).

From the stochastic simulations, an angular intensity is determined as the number of simulated photons exiting at a given angle as a fraction of the total photons simulated. The shapes of the simulated intensity, I_{sim}, and the measured intensity, $\langle I(t)\rangle_\theta$, as a function of angle are similar, despite differences in magnitude. Similar to Fahimi et al., we determine an experimental constant β_{exp} to scale the simulated intensity to match the measured intensity for the calibration samples [19]. To do this, we minimize the total mean squared error between each simulated and measured intensity curve in log-space and take the average across all calibration samples, obtaining a value of β_{exp}~1.1 × 10^8 Hz. Fig. 4B shows measured and simulated intensity curves scaled by β_{exp} as a function of angle for five calibration samples. As shown, the average value of β_{exp} adequately scales simulation intensities to match measured intensities for both polystyrene and SiO_2 suspensions. In Fig. 4C, we plot the determined values of β_{exp} for all calibration samples as a function of l^* and grouped by size and refractive index of the particles used (inset, Fig. 4C). β_{exp} showed no statistical dependence on any of these factors and implied that over these ranges of particle sizes and refractive indexes it was a function of the experimental apparatus only.

The statistical independence of β_{exp} on l^*, particle size, and particle refractive index suggested that it could be used to determine l^* from intensity data alone for dispersions with characteristics outside of those used in calibrations. To test this, we measured the intensity at three different angles (30, 90, and 150 degrees) for suspensions made with 4.30 μm SiO_2 and 3.0 μm polystyrene. These suspensions represented a fourfold and threefold increase in size over the largest used in calibration. We then scaled the entire library of simulated intensity curves for each l^* by β_{exp} and determined l^* to be the intensity curve that minimized the squared error between simulated intensity and measured intensity. Results from this fitting procedure are shown in Fig. 4D. Despite the dispersed particles lying outside the range of calibration particle sizes, the scaled intensity curves align well with the measured intensity curves. We theorize that the multi-angle fitting approach approximates generating an intensity curve over differing sample thicknesses in the classical semi-infinite experimental geometry, which has been used to obtain robust estimates for l^* given a calibration transmission intensity [20]. In contrast, however, the multi-thickness approach requires multiple sample cuvettes, whereas we only require a single sample cell and instead change the location of the detector.

3.4. Extracting and analyzing MSD

In a previous study, we showed how DWS could be employed to disentangle Brownian and ballistic creaming motions in emulsions, utilizing realistic Monte Carlo simulations [18]. Here we show a more general approach to extract the mean squared displacement of scattering centers: once l^* is determined from the intensity curve for a sample, it can be used in Eq. 2 and the mean squared displacement, $\langle \Delta r^2(\tau)\rangle$, can be numerically solved for. Importantly, the error originating from $g_2(\tau)$ is propagated to the mean squared displacement and is incorporated into the fitting routines. Physical properties exhibited by scattering centers are found by utilizing a model for the extracted mean squared displacement. Using an improper model, however, can cause incorrect conclusions to be drawn about the dynamics of the system. To circumvent this, the extracted mean squared displacement is fit in successive stages.

First, only the physically relevant region, found as shown in Fig. 3C, of the field autocorrelation function is used to fit the anomalous diffusion equation, $\langle \Delta r^2(\tau)\rangle = 6K_\alpha \tau^\alpha$. Depending on the value of the exponent, α, the major regime of scattering center motion can be determined. Fig. 5A shows the expected shape of the anomalous diffusion curve exhibiting super-diffusive (top line, $\alpha > 1$), Brownian (middle line, $\alpha = 1$), and sub-diffusive (bottom line, $\alpha < 1$) motion. Thus, only if α contains 1 within its 95% confidence interval can the Brownian diffusion model be used. Elsewhere, a better suited model must be used. In Fig. 5B, the extracted mean squared displacement of an 8.7 wt% 4.3 μm SiO_2 suspension is shown, along with fit lines constrained for different values of α. The dashed line represents the best fit Brownian curve, where significant deviations from the determined data can be seen. Similarly, the sub-diffusive line with $\alpha = 0.85$ also shows significant deviation to the data. Finally, an unconstrained fit of the anomalous diffusion equation yields a value of $\alpha = 1.48$.

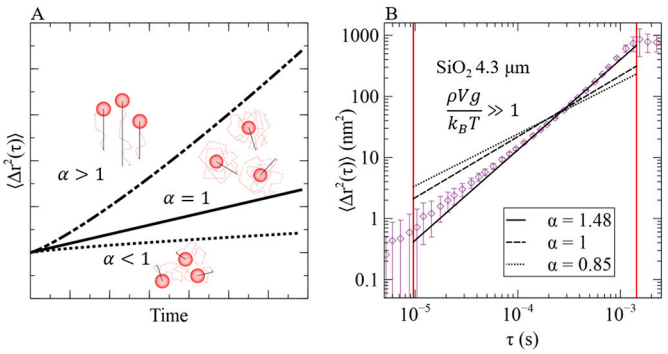

Fig. 5. Dynamic regimes of the mean squared displacement. A) theoretical shapes of the anomalous diffusion curve for $\alpha > 1$, $\alpha = 1$, $\alpha < 1$ corresponding to super-diffusive, Brownian, and sub-diffusive motion, respectively. B) Extracted mean squared displacement of an 8.7 wt% 4.3 μm SiO_2 suspension (symbols). The lines show different theoretical fits to the anomalous diffusion equation by constraining the value of α, where the solid black line is the best-fit value of α.

3.5. Particle sizing in dense suspensions

We conclude by validating our approach on SiO_2 and polystyrene suspensions, prepared as described in Section 2.1. Additionally, we compare the results obtained by approximating the cylindrical cuvette as a semi-infinite slab using the analytical form of $g_1(\tau)$. The extracted mean squared displacement from both Eq. 2 and the analytical form are shown in Fig. 6 for an 8.7 wt% 4.3 μm SiO_2 dispersion (A) and a 2.5 v% 3.0 μm polystyrene dispersion (B), both at 90°.l^* was determined using the multiple angle intensity fit as described in Section 3.3. For the analytical $g_1(\tau)$, the thickness, L, was calculated geometrically and is shown in Fig. 2A.

Mean squared displacements were fit using Eq. 6 in Bellour et al. to capture all ranges of possible dynamics, since both samples exhibited non-Brownian dynamics due to their large size [28]. To assess the validity of of our approach, we compare the diameter of dispersed particles determined by the mean squared displacement fit to manufacturer specifications and the diameter determined by microscopy, shown in Fig. 6C and D. The SiO_2 dispersions show an upward sloping curve at long lag times due to the density contrast with waster and had α values ranging from 1.40 to 1.50. While the polystyrene suspensions exhibited less pronounced upward curvature, the dynamics were still faster than Brownian diffusion, with α values ranging between 1.08 and 1.10. In both instances, the transmission approximation shows relatively good agreement with Eq. 2 at short lag times, before positive divergence at long lag times. The divergence at later times is likely due to the differences in the path length distribution shown in Fig. 2B.

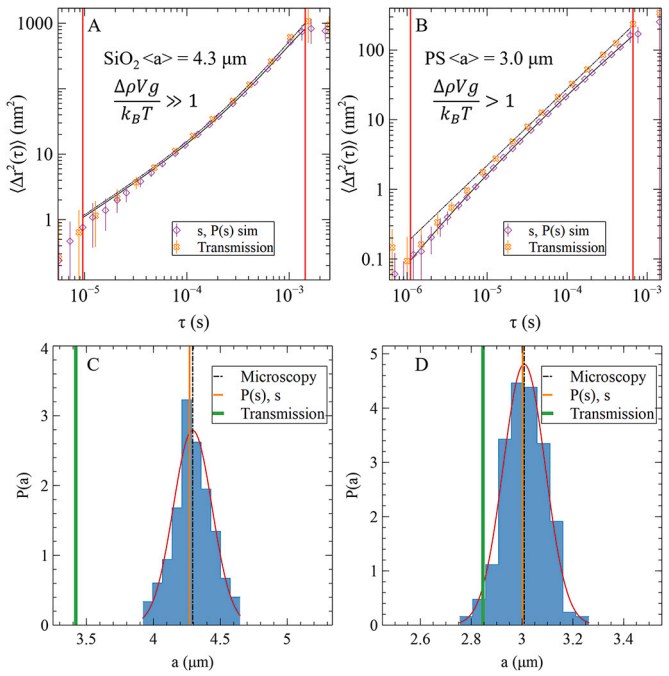

Fig. 6. Determining size of suspension particles using the systematic workflow. A) Extracted mean squared displacement using the stochastically simulated P (s), s in $g_1(\tau)$ at 90 degrees (diamonds) and the analytical form of $g_1(\tau)$ with the 90 degree L equivalent for an 8.7 wt% 4.3 μm SiO_2 particle dispersion. B) Extracted mean squared displacement using the stochastically simulated P(s), s in $g_1(\tau)$ at 90 degrees (diamonds) and the analytical form of $g_1(\tau)$ with the 90 degree L equivalent for a 2.5 v% 3.0 μm polystyrene particle dispersion. All lines are fit using Eq. 6 in Bellour et al. C) Size histogram of the 4.3 μm SiO_2 particles determined via microscopy. D) Size histogram of the 3.0 μm polystyrene determined via microscopy. In both C and D, black vertical dashed lines represent the average size determined via microscopy, the orange vertical lines are the size extracted by fitting the mean squared displacement extracted from the P(s), s simulated $g_1(\tau)$, and the green vertical lines are the extracted size of the particles by fitting the mean squared displacement of the analytical form of $g_1(\tau)$. Finally, both histograms have a red Gaussian curve overlaid to show uniformity. (For interpretation of the references to colour in this figure legend, the reader is referred to the web version of this article.)

Table 1
Values of extracted size of SiO_2 and polystyrene suspensions. DLS determined size of the polystyrene particles was 3.09 ± 0.19 μm. The SiO_2 particles were not able to be analyzed by conventional DLS because of the sedimentation velocity.

Material	P(s), s Simulation	Transmission	Microscopy	Manufacturer Specification
SiO_2	$\langle a \rangle = 4.26 \pm 0.14 \mu m$	$\langle a \rangle = 3.41 \pm 0.08 \mu m$	$\langle a \rangle = 4.29 \pm 0.15 \mu m$	$\langle a \rangle = 4.30 \pm 0.05 \mu m$
Polystyrene	$\langle a \rangle = 3.05 \pm 0.25 \mu m$	$\langle a \rangle = 2.63 \pm 0.29 \mu m$	$\langle a \rangle = 2.98 \pm 0.07 \mu m$	$\langle a \rangle = 3.03 \pm 0.03 \mu m$

Despite the comparable shapes exhibited by the transmission approximation to Eq. 2, there are significant deviations in the particle sizes determined by mean squared displacement fitting. In Fig. 6C and D, the particle size from fitting to each curve is shown compared to microscopy sizing. The average sizes from each method are summarized in Table 1, as well as manufacturer specifications. Using the stochastically modeled P(s), the particle sizes are in good agreement with microscopy and manufacturer specifications. The transmission approximation, however, yielded particle sizes much lower in comparison, likely due to the increased curvature of the extracted mean squared displacement curves.

4. Conclusion

Diffusing wave spectroscopy (DWS) offers a powerful technique to analyzing optically dense systems. Herein, we report a method of analysis offering significant accuracy in determining particle dynamics on a non-standard DWS instrument. Specifically, our approach standardizes a work flow for extracting and analyzing the mean squared displacement of dispersed phase systems, yielding accurate particle sizing in dense suspensions. The method utilizes a multi-angular fitting approach to determine l^* independent of particle dynamics. Additionally, the standard error from photon correlation is calculated and propagated through the analysis to provide statistical bounds on all extracted parameters. The error is further used to determine a physically significant region of the mean squared displacement, insuring noise does not influence interpretation of results. The method proposed exhibits accuracy that is not typically observed in DWS measurements, which ranges between ±5–8%, allowing extension to particle sizing in dense systems [21,29]. We anticipate that the workflow exemplified on suspensions can be utilized in analyzing other dispersed systems, such as emulsions, with greater precision than other standard analysis techniques.

CRediT authorship contribution statement

Robert E. McMillin: Conceptualization, Methodology, Visualization, Data curation, Writing – original draft, Writing – review & editing, Formal analysis, Software, Investigation. **Davide Orsi:** Software, Conceptualization, Methodology. **Luigi Cristofolini:** Conceptualization, Methodology, Writing – review & editing. **James K. Ferri:** Conceptualization, Methodology, Formal analysis, Investigation, Writing – original draft, Writing – review & editing, Supervision, Project administration, Funding acquisition.

Declaration of Competing Interest

James K. Ferri reports financial support was provided by NASA (Grant 80NSSC18K0453). Luigi Cristofolini reports financial support was provided by European Space Agency (Contract 4000128643/19).

Data availability

Data will be made available on request.

Appendix A. Supplementary data

Supplementary data to this article can be found online at https://doi.org/10.1016/j.colcom.2022.100641.

References

[1] P.T. Wong, S.H. Wang, S. Ciotti, P.E. Makidon, D.M. Smith, Y. Fan, C.F. Schuler, J. R. Baker, Mol. Pharm. 11 (2014) 531–544.
[2] I.A.M. Appelqvist, M. Golding, R. Vreeker, N.J. Zuidam, in: J.M. Lakkis (Ed.), In *Encapsulation and Controlled Release Technologies in Food Systems*, 2nd ed., John Wiley and Sons Ltd, 2019, p. 177. Chapter 6.
[3] S.A. Rizvi, A.M. Saleh, Saudi Pharm. J. 26 (2018) 64–70.
[4] F. Gambinossi, S.E. Mylon, J.K. Ferri, Adv. Colloid Interf. Sci. 222 (2015) 332–349.
[5] C. Grapentin, S. Barnert, R. Schubert, PLoS One 10 (2015) 1–12.
[6] D. Pine, D.A. Weitz, J.X. Zhu, E. Herbolzheimer, Dynamic Light Scattering te Method and Some Applications 51 (1990) 2101–2127 0199000510180.
[7] N. Isert, G. Maret, C.M. Aegerter, Colloids Surf. A Physicochem. Eng. Asp. 473 (2015) 40–45.
[8] A.D. Gopal, D.J. Durian, Phys. Rev. Lett. (1995) 75.
[9] A.J. Liu, S. Ramaswamy, T.G. Mason, H. Gang, D.A. Weitz, Phys. Rev. Lett. 76 (1996) 3017–3020.
[10] F. Salerni, D. Orsi, E. Santini, L. Liggieri, F. Ravera, L. Cristofolini, Colloids Surf. A Physicochem. Eng. Asp. (2019) 580.
[11] D.A. Weitz, D.J. Pine, Dynamic Light Scattering: The Method and Some Applications, 1st ed., Clarendon Press, 1993 (Chapter 16).
[12] J. Xu, A.K. Jahromi, C. Yang, APL Photon. (2021) 6.

[13] D. Ferreira, R. Bachelard, W. Guerin, R. Kaiser, M. Fouché, Am. J. Phys. 88 (2020) 831–837.
[14] D.A. Weitz, H. Gang, D.J. Pine, J.X. Zhu, D.J. Durian, Phys. Scr. 1993 (1993) 610–621.
[15] C. Sun, T. Wu, R. Liu, B. Liang, Z. Tian, E. Zhang, M. Zhang, Food Hydrocoll. 51 (2015) 512–518.
[16] Z. Zhao, M. Corredig, J. Dairy Sci. 99 (2016) 2588–2593.
[17] L.F. Rojas, M. Bina, G. Cerchiari, M.A. Escobedo-Sánchez, F. Ferri, F. Scheffold, Eur. Phys. J. Special Top. 199 (2011) 167–180.
[18] V. Lorusso, D. Orsi, F. Salerni, L. Liggieri, F. Ravera, R. McMillin, J. Ferri, L. Cristofolini, Adv. Colloid Interf. Sci. 288 (2021), 102341.
[19] Z. Fahimi, F.J. Aangenendt, P. Voudouris, J. Mattsson, H.M. Wyss, Phys. Rev. E 96 (2017) 1–17.
[20] D.J. Durian, D.A. Weitz, D.J. Pine, Science 252 (1991) 686–688.
[21] C. Zhang, M. Reufer, D. Gaudino, F. Scheffold, Korea Austral. Rheol. J. 29 (2017) 241–247.
[22] A. Kim, W.B. Ng, W. Bernt, N.-J. Cho, Sci. Rep. 9 (2019) 1–14.
[23] C. Fraschini, G. Chauve, J.-F. Le Berre, S. Ellis, M. Méthot, B. O'Connor, J. Bouchard, Nordic Pulp Paper Res. J. 29 (2014) 31–40.
[24] W. Anderson, D. Kozak, V.A. Coleman, Å.K. Jämting, M. Trau, J. Colloid Interface Sci. 405 (2013) 322–330.
[25] K. Schätzel, Quantum Optics: J. Eur. Optic. Soc. B 2 (1990) 287–305.
[26] D. Orsi, F. Salerni, E. Macaluso, E. Santini, F. Ravera, L. Liggieri, L. Cristofolini, Colloids Surf. A Physicochem. Eng. Asp. (2019) 580.
[27] R. Metzler, J.H. Jeon, A.G. Cherstvy, E. Barkai, Phys. Chem. Chem. Phys. 16 (2014) 24128–24164.
[28] M. Bellour, M. Skouri, J.P. Munch, P. Hébraud, Eur. Phys. J. E 8 (2002) 431–436.
[29] LS Instruments. https://lsinstruments.ch/en/theory/diffusing-wave-spectroscopy-dws/dws-particle-sizing.